Fluid-driven seismic swarms in the Gripp valley (Haute-Pyrénées, France)

Benoit Derode, Alisson Gounon, Jean Letort, Matthieu Sylvander, Alexis Rigo, Sébastien Benahmed, Frank Grimaud, Soumaya Latour, Hélène Pauchet, Alvaro Santamaria

Geophysical Journal International

Geophys. J. Int. (2023) **234,** 1903–1915
Advance Access publication 2023 April 26
GJI Seismology

https://doi.org/10.1093/gji/ggad175

Fluid-driven seismic swarms in the Gripp valley (Haute-Pyrénées, France)

Benoit Derode [1], Alisson Gounon [1], Jean Letort,[1] Matthieu Sylvander,[1] Alexis Rigo,[2] Sébastien Benahmed,[1] Frank Grimaud,[1] Soumaya Latour,[1] Hélène Pauchet[1] and Alvaro Santamaria [3]

[1] *IRAP, UMR* 5277, *Université Toulouse* 3, *CNRS, CNES, UPS,* 31400 *Toulouse, France. E-mail: bderode@irap.omp.eu*
[2] *Laboratoire de Géologie, UMR* 8538, *École Normale Supérieure, PSL,* 75005 *Paris, France*
[3] *GET, UMR* 5563, *Université Toulouse* 3, *CNRS, IRD, CNES, UPS,* 31400 *Toulouse, France*

Accepted 2023 April 20. Received 2023 April 19; in original form 2022 August 17

SUMMARY

An unusual seismic activity has recently occurred in the Gripp valley, located in the central part of the French Pyrenees. Since spring 2020, two new swarms appeared, clearly outside the usual location of the seismicity in this area. On 20 September 2020, almost concomitantly with the activation of the second seismic swarm, a hole suddenly opened in the bed of a local river, the Adour de Payolle. This hole drained the water from the river, which dried up over 500 m. We follow and study the spatial and temporal evolution of these clusters, using four temporary stations deployed a few days or months after the beginning of the crisis to complete the regional network. These additional data lead to the construction of a comprehensive catalogue of more than 4900 earthquakes, using both a template matching approach and a deep-learning based phase picking method to complete and improve the initial catalogue available from the French seismological agency. This allows highlighting a slow and clear migration of the seismicity during 1 yr. Precise absolute and relative event locations reveal a dipping faulting structure, confirmed by the focal mechanism estimated for the highest magnitude event of the sequence (M_L 3). We propose to explain the observed migration of the seismicity by deep fluids going up through a newly discovered faulting structure.

Key words: Machine learning; Earthquake source observations; Seismicity and tectonics; Seismic swarm; Fluid flow.

1 INTRODUCTION

At the boundary between the Eurasian and Iberian lithospheric plates, the Pyrenees has a moderate and well-documented crustal seismicity (see Sylvander *et al.* 2021, for a review). This seismicity is preferentially organized in the form of clusters, more intense in the central and western parts of the chain (Sylvander *et al.* 2021). Since spring 2020, two new seismicity clusters have appeared on the periphery of the active regions highlighted by Sylvander *et al.* (2021) in the central French Pyrenees. They are located in the Gripp valley and are not geographically connected to the clusters identified until then (Fig. 1a, red versus blue dots). The first of these two swarms (A, Figs 1a and b) was activated in June 2020, and the second (B, Figs 1a and b) in September 2020, 3–4 km further to the northwest. This second swarm mobilized hundreds of low magnitude events (between 0 and 3.5 on a local scale).

On 20 September 2020, almost simultaneously with the appearance of the second swarm (letter B in bold type, Figs 1a and b), an unusual hydrological phenomenon attracted the attention of the local population and media. A cavity suddenly opened in the bed of a local mountain river, the Adour de Payolle, swallowing the water of the river, which went dry for more than 500 m downstream (Barréjot 2020).

The distance between the seismicity and this hole is quite large (8–10 km), but the simultaneity of these unusual phenomena raises questions about a possible link between them. Furthermore, the opening of such cavities on this river was previously observed in 1773, 1777 and 1816 (Adisson 2008). This author proposed a direct relationship between these cavities and some earthquakes felt by local populations a few days before the openings. Unfortunately, no instruments were available at that time, and this question still remains open. If no 'major' event ($M_L > 4$) was detected in this area a few days before the opening of the hole, the existence of a possible link with the activation of the two swarms should be considered and studied.

It is known that crustal fluids can play a major role in the earthquake cycle (Toutain & Baubron 1999). Reciprocally, seismicity can locally impact fluid circulation (Derode *et al.* 2013, 2015) as

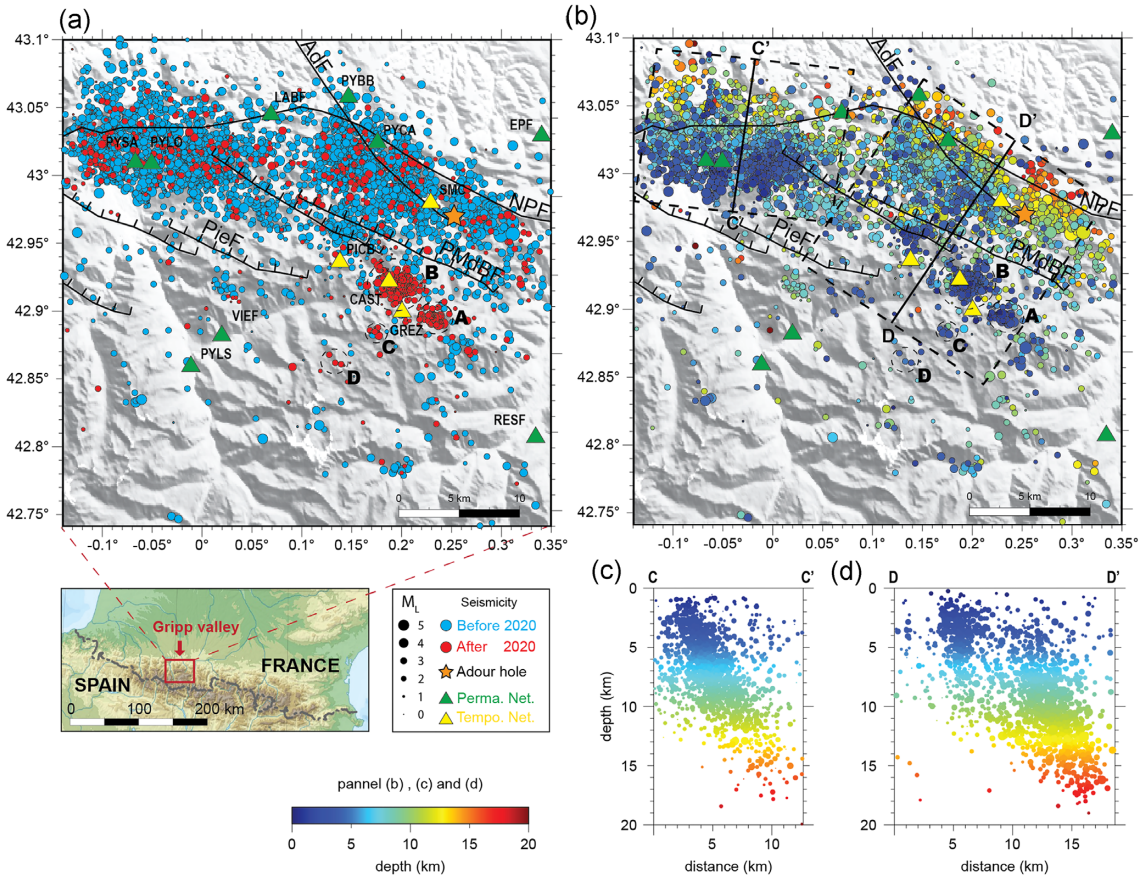

Figure 1. BCSF-RENASS-OMP merged seismic catalogue for the period 1997–2021. (a) 1997–2019 (blue dots) and 2020–2021 (red dots). The main faults are taken from Lacan & Ortuño (2012) and represented: the NPF (North Pyrenean Fault), the PMdB Fault (Pic du Midi de Bigorre Fault), the AdF (Adour fault) and the PieF (Pierrefitte Fault). Four unusual seismic swarms occurring from 2020 are tagged with letters A, B, C and D. (b) Same catalogue for the whole 1997–2021 period, with colour indicating the depth of the seismic events. (c–d) Cross-sections of the boxes delimited in (b).

already seen in the Pyrenees for the Ogeu spring (Toutain *et al.* 2006). Crustal instabilities (e.g. faults) can also appear during tectonic loading, even with small stress/strain perturbations (Toutain & Baubron 1999). We therefore aim to evaluate if crustal fluids can consistently explain both the hole opening and the seismicity for the Gripp area.

Understanding the seismic properties of this area and this ongoing seismic crisis is even more crucial with respect to seismic hazard. In the past centuries, the region has experienced several major earthquakes, among which the strongest felt earthquake in the French Pyrenees, the so called Bagnères-de-Bigorre earthquake, that occurred on the 21st June 1660 and displayed a maximum macroseismic intensity estimated between VIII and IX (MartinGrasset 1969).

In this study, we propose a first analysis of the main properties of the swarms. In particular, we follow their spatial and temporal evolution, using four temporary stations deployed shortly after the beginning of the crisis to complete the regional network (Figs 1a and b, yellow triangles). We build a comprehensive catalogue of more than 1300 earthquakes detected and located using a deep learning-based phase picking method and the NonLinLoc inversion algorithm (Lomax *et al.* 2000; Lomax *et al.* 2014), respectively, to complete and improve the initial French national BCSF-RENASS-OMP merged catalogue available for this area. A relative event relocation was also conducted, highlighting a northeastward dipping faulting structure, confirmed by the focal mechanism estimated for the highest magnitude event of the cluster B (Figs 2a–d). We finally completed this study by a template-matching approach applied on the different swarms, leading to the detection of more than 4900 events of lower magnitudes. The results show a slow and clear migration of the seismicity towards the southwest during more than 1 yr. We finally discuss possible mechanisms that could explain this observed migration pattern.

2 DATA

2.1 Initial BCSF-RENASS catalogue and observations

The French national BCSF-RENASS catalogue reports 537 events between 1 January 2020 and 1 October 2021 in the region of the swarms, with local magnitudes M_{Lv} between 0.1 and 3.1. During this period, the seismicity is clustered mainly in two patches covering each ∼10 km^2 and distant from 4 km (clusters A and B, Fig. 1), at the south of the usual background seismicity. Two smaller clusters (C and D, Fig. 1), with only a few events, can also be noted. At first sight, these four clusters are not associated to known outcropping tectonic structures. The main faults known in the region are: (1) the North Pyrenean Fault, a highly metamorphized and segmented structure that separates the Pyrenean Axial Zone from the so-called North Pyrenean Zone and whose present seismic activity is debated; (2) the Adour Fault along the Adour River that disappeared in September 2020 and which does not show any geomorphological expression

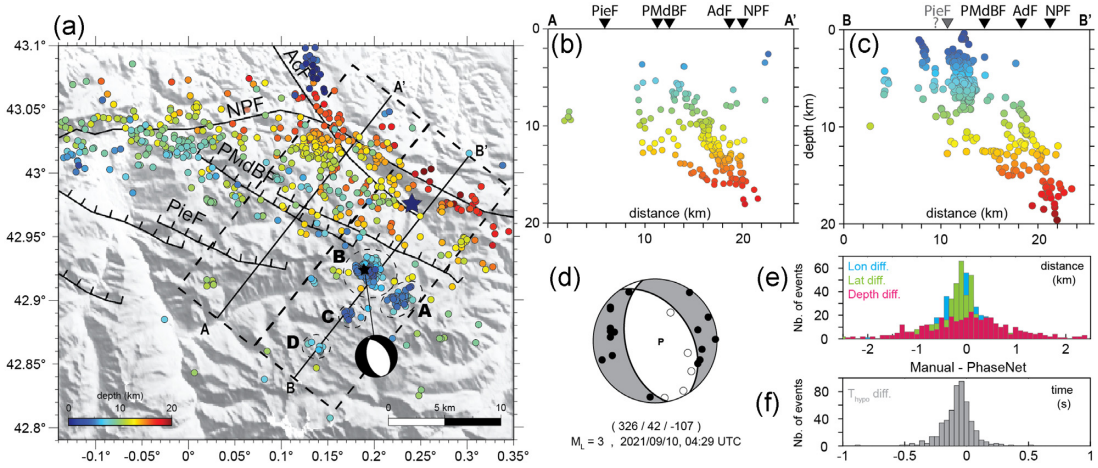

Figure 2. (a) Location map of earthquakes (2020.01.01 to 2021.10.01) obtained through our automatic procedure (PhaseNet + Real, Section 3). Dark-blue star marks the subsiding hole in the Adour River. Dashed-black lines represent the section tracks of (b)–(c). (b) Cross-section through the AdF-NPF-PMdBF-PieF fault-complex. (c) Cross-section through the newly appeared seismic swarms. (b–c) Outcrops of the pre-existing faults are indicated. The mean dip of the seismicity in (b) could correspond to the PMdBF fault system. In (c), the subvertical dip of the deep seismicity could highlight the deep part of the AdF. However, the surface faulting is complex and there is no direct evidence to link the seismicity to a specific outcropped fault. (d) focal mechanism of the strongest event occurring within the swarms (2021.09.10, 04:29 UTC, M_L 3). (e–f) histograms of event location differences (e) and origin time differences (f), for hypocentral locations estimated from manual and automatic pickings.

and (3) the Pic du Midi and Pierrefitte normal faults, two parallel faults, oriented west northwest—east southeast (Fig. 1). See Lacan & Ortuño (2012) for a review.

2.2 Seismic recordings

In order to better understand this seismic sequence, we have collected the complete time series from all the closest permanent stations of the Résif seismic network (Résif 1995a;b), that includes broad-band velocimetric and accelerometric stations. All the stations are located within 50 km of the cluster B (green triangles, Fig. 1). In order to reduce uncertainties on the locations, we complemented this network by four temporary short-period velocimeters (yellow triangles, Fig. 1). The complete monitoring system therefore included up to 15 three-component stations, sampled at 100 Hz (Table 1).

2.3 Velocity model

We used the 1-D velocity model (Table 2) from Pauchet *et al.* (1999) for earthquake location. The V_P/V_S ratio has been modified and fixed to 1.72 instead of the initial value of 1.75. This change was induced by the estimation of a local value thanks to the construction of a Wadati diagram (Wadati 1933) using an accurate manual *P* and *S* pickings of all events of the BCSF-RENASS catalogue.

3 FOCAL MECHANISM ESTIMATION FOR THE 2021-09-10 EVENT

The strongest event (M_{Lv} 3) of the 2-yr sequence occurring inside the clusters was the 10 September 2021 (04:29 UT), estimated at a depth of 6.2 km (Figs 2a and d). A focal mechanism based on *P*-wave polarities could be determined for this event, thanks to a good azimuthal coverage of 23 permanent and temporary stations. It indicates clear normal faulting (Figs 2a–d). The ENE dipping nodal plane (strike 326°, dip 42°, rake −107°) is most likely the activated fault plane, since it is the most consistent with the dipping of the seismicity (Fig. 2c).

4 EARTHQUAKE DETECTION AND LOCATION FROM DEEP LEARNING-BASED APPROACH

A fully automated deep-learning based method (PhaseNet, Zhu & Beroza 2019) is first used to detect new earthquakes missed by the BCSF-RENASS catalogue, by tracking *P* and *S* waves arrivals, relying on the data from the four temporary short-period velocimeters, and from the whole permanent seismic network available.

PhaseNet (Zhu & Beroza 2019) automatically picks regional *P* and *S* wave arrivals from three-components seismograms, based on a Deep Neural Network method (DNN). This algorithm has recently shown its ability in identifying regional seismic phases in different seismotectonic contexts (Münchmeyer *et al.* 2021; Ammirati *et al.* 2022; Retailleau *et al.* 2022). For the Pyrenees area, Derode *et al.* (2021) also proved the efficiency of this automatic picking method. They show that differences between PhaseNet and manual time phase-picks are smaller than 0.2 s for both *P* and *S* waves, which is similar to the difference expected between picks provided by different analysts working on the same database of seismograms.

The time series of all stations are scanned for the period between 2020.01.01 and 2021.10.01 and *P* and *S* phases are automatically picked, with a minimal phase probability threshold of 0.3. Then, we use the Rapid Earthquake Association and Location algorithm (REAL, Zhang *et al.* 2019) to associate the seismic phases from the different stations and to estimate a preliminary and rough location. By using pre-calculated time-arrival tables for each source–station pair on a predefined theoretical rough grid (0.02° × 0.02° × 2 km), this rapid grid-search based algorithm provides a first catalogue of suspected seismic events. To reduce the number of false positives events, we required a minimum of three *P* and three *S* arrivals. A last step of absolute relocation is performed, using the stochastic NonLinLoc inversion method, relying on the Pyrenean 1-D velocity model (section 1). Finally, we remove the events displaying vertical

Table 1. Temporary and permanent stations used in this study.

Name	Network—Type of instrument	Longitude (°)	Latitude (°)	Distance from the second (B) seismic swarm (km)	Set up date
SMC	Temporary-SP velocimeter	0.2315	42.9808	7	15/10/2020
CAST	Temporary-SP velocimeter	0.1902	42.9222	0	02/12/2020
PICB	Temporary-SP velocimeter	0.1408	42.9371	4	30/04/2021
GREZ	Temporary-SP velocimeter	0.2034	42.8999	3	22/07/2021
LABF	OMP-BB velocimeter	0.0727	43.0459	17	Permanent
VIEF	OMP-BB velocimeter	0.0229	42.8825	14	Permanent
MELF	OMP-BB velocimeter	0.7575	42.8717	47	Permanent
RESF	OMP-BB velocimeter	0.3379	42.8070	18	Permanent
REYF	OMP-BB velocimeter	−0.3933	43.0683	50	Permanent
PYBB	OMP-BB velocimeter	0.1489	43.0586	15	Permanent
PYLO	OMP-BB velocimeter	−0.0493	43.0969	27.5	Permanent
PYSA	OMP accelerometer	−0.066	43.0992	28	Permanent
PYCA	BRGM accelerometer	0.1771	43.0236	11	Permanent
PYLS	BRGM accelerometer	−0.0085	42.8603	18	Permanent
EPF	CEA-SP velocimeter	0.34	43.0308	17	Permanent

Table 2. Velocity model used in this study, modified from Pauchet *et al.* (1999).

Depth (km)	Pyrenean 1-D velocity model V_P (km s^{-1})	V_S (km s^{-1})
0–1	5.5	3.2
1–4	5.6	3.26
4–11	6.1	3.55
11–34	6.4	3.72
>34	8.0	4.5

and horizontal uncertainties greater than 2.5 km, and with RMS above 0.2 s. A total of 1305 events are kept (see Fig. 2) and located, from which 795 are included in the box of interest (42.8°N–43°N–0.1°E–0.3°E) containing the initial 537 events of the BCSF-RENASS catalogue. A significant increase in the catalogue completeness is thus achieved (around 50 per cent more events).

To evaluate and ensure the accuracy of the automatic picks provided by the PhaseNet approach, we compare them to the picks of two other independent picking methods: (1) the picks provided by the BCSF-RENASS analysts and (2) a careful manual repicking of the 537 events from the BCSF-RENASS catalogue accomplished by the authors for this study. For the comparison PhaseNet versus Manual picking, we added the new manual picks from the four temporary stations. for the 537 events The comparison is carried out for the three high-quality broad-band stations LABF, VIEF and RESF of the permanent network. The mean time differences between analysts and automatic picks are all small (Δt_{An}—$\Delta t_{\mathrm{PhNt}} < 0.1$ s for both *P* and *S* waves, Fig. 3), which indicates a good quality of the automatic picks and validates their use.

We also compare the new manual relocations obtained by applying the same relocation procedure (NonLinLoc with our 1-D velocity model), with those from the global automatic procedure (automatic picking with PhaseNet, phase association with REAL and seismic location with NonLinLoc). We found average differences in latitude, longitude and depth of 0.11 ± 0.45 km, 0.15 ± 0.48 km and 0.07 ± 1.51 km, respectively (Figs 2e and f). These small differences illustrate the efficiency of our automatic detection and location method.

Finally, once the absolute relocation based on our automatic picking procedure is achieved, and in order to better constrain the internal structure of the four observed swarms (A, B, C, D; Figs 1 and 2), we perform a relative relocation using the double difference HYPODD algorithm (Waldhauser 2001; Waldhauser & Ellsworth 2002), particularly relevant in the context of cluster analyses. The automatic PhaseNet selected picks are used as absolute catalogue times and waveforms are cross-correlated to produce a set of high-quality differential times. Cross-correlations (CC) are calculated on 2 s time windows centred on the catalogue (PhaseNet) picks. The correlation threshold is fixed at a conservative value of 0.7 for both *P* and *S* waves. We furthermore impose that both P and S arrivals correlate at this level in order to take into account the CC differential times at one station. This yields 23 716 pairs of events for which at least one station provided CC differential times, for a total of 33 115 P and the same amount of *S* differential times. This volume of data leads to a precise relocation of the PhaseNet-catalogue events. We call this approach *HypoDD* in the next paragraphs/sections.

5 SPATIAL DISTRIBUTION OF THE OBSERVED SEISMICITY

At a large scale (∼600 km^2, Figs 2a–c), a general dipping of the seismicity towards the northeast is observed (Azim ∼30°, dip ∼40°), which is consistent with the long-term features of the seismicity (Sylvander *et al.* 2021). Most of the deep seismicity (>15 km) is found below the North Pyrenean Fault (red dots, Fig. 2a), with a deeper part East of the 'Adour hole'. This lateral deepening will be discussed in the Section 8. Our absolute automatic detection and location approach (Section 3) also allows to highlight and confirm the presence of the two small clusters (C, D, Figs 1a–b and 2a), detecting new events inside these clusters.

Our *HypoDD* relative relocations (Fig. 4) show tight clusters A, B, C and D, and confirm a dipping of the seismicity for cluster B towards ENE (see Section 7). Cluster A seems to be separated into two subclusters (Figs 4c and f). The first one is shallow, around 3 km depth, and the second one deeper, around 7–8 km depth, but with exactly the same epicentral locations. However, no temporary stations were operating during the activation of this cluster (June to August 2020), and we will show later that this observed double depth range could results from a bias in the location procedure, and that all events could be in fact in a same depth range.

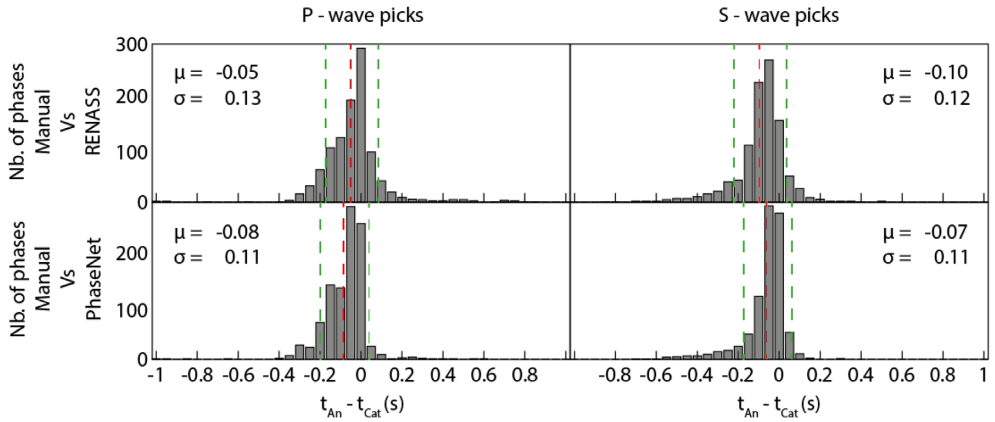

Figure 3. Histogram of *P* and *S* residuals for both Manual/RENASS and Manual/PhaseNet picking comparisons. In each panel, t_{An} corresponds to our manual reference time, and t_{Cat} to the RENASS time (upper part) and the PhaseNet time (lower part). The red dashed lines indicate the mean (μ) and the green dashed lines indicate the limits of the standard deviation (σ).

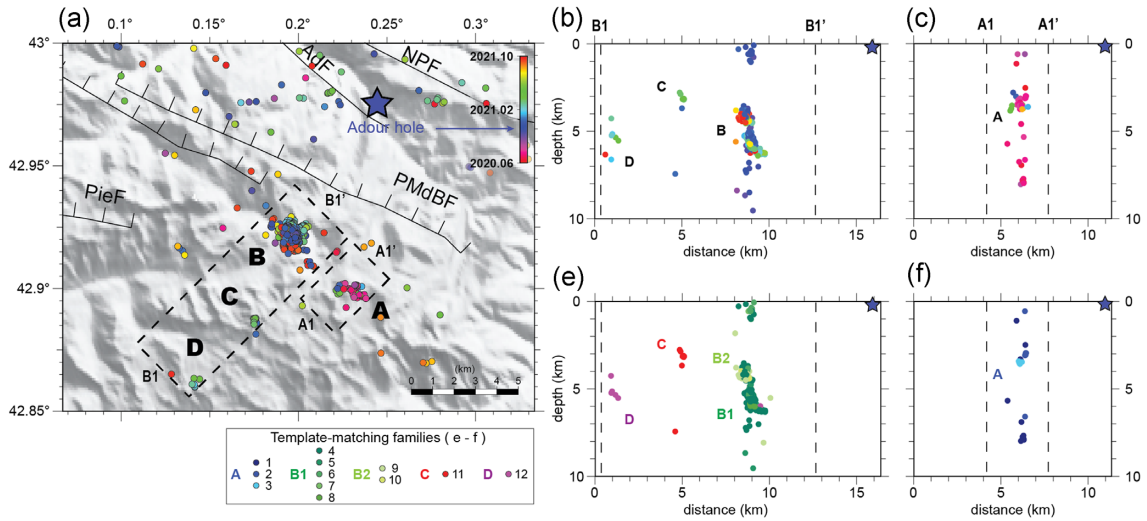

Figure 4. Map and cross-sections of the 2020–2021 PhaseNet-*HypoDD* relocated seismicity (see text). (a) Large scale seismicity map, colours indicating the date of the events. (b–c) Cross-sections along the azimuth perpendicular to the delimited zones B1–B1' and A1–A1' in (a). The blue star indicates the position of the Adour hole. (e–f) Same as (b–c), but with colours indicating to which one of the 12 different families detected by template-matching (described in Table 3) belong the events of clusters A to D.

6 TEMPORAL EVOLUTION OF THE CLUSTERS IDENTIFIED BY TEMPLATE-MATCHING

In the previous section, we highlighted the presence of four clusters in the studied region. Clusters can also be defined based on their waveform similarity (e.g. Baisch *et al.* 2008; Gao *et al.* 2021; Schaff & Richards 2011; Hatch *et al.* 2020). A preferred method to better estimate the temporal evolution of the seismicity within these clusters consists in improving our number of detections for a specific location by using seismic templates, and operating a systematic search of the similar waveforms within the noisy signal, the so-called Template-Matching technique. In the following, we will describe this classification and systematic search procedure that allowed us to densify our catalogue at the level of the clusters identified in the previous section.

For the two temporary stations GREZ and SMC, as well as for the two permanent broad-band stations VIEF and LABF, a common procedure of template matching is applied. For a given station, all the events (localized by our PhaseNet-HypoDD procedure, Section 3) are selected. Their associated waveforms are bandpassed filtered between 5 and 20 Hz. For all stations the waveforms are cut 0.5 s before the *P*-wave arrival, 11.5 s after, and cross-correlated. If waveforms from at least five events have their cross-correlation coefficients above 0.7, these events are considered as a family of events having similar waveforms. For each of these identified families, a template is then estimated, its composite waveform being the average waveform of all of its family individual waveforms. The exact same procedure is applied for the four stations GREZ, SMC, VIEF and LABF. We find 23 templates for the station VIEF, 22 for LABF, 15 for SMC and 4 for GREZ.

The temporary station CAST is treated slightly differently as it is located just above the main cluster B and thus records closer events, only a few kilometres away from the station. To take into account this proximity, the records from the CAST station are filtered with a higher frequency band 10–40 Hz to allow the detection of smaller and closer events. The chosen time window is shorter (0.5 s before the *P* arrival and 7.5 s after for a total 8 s duration), and the minimum

cross-correlation coefficient is set to 0.8. 11 families/templates are finally identified for the CAST station.

Then, for each of these five stations taken independently, the continuous time series are scanned, windowed with a time step of 2 s, and correlated with the waveforms of each of their template events. If a correlation coefficient reaches 0.4 for a given time window (0.5 s for CAST), a new detection is assumed, and the corresponding event is added to the family that has the highest correlation coefficient. This approach allows the detection of 11 018 new events, all related to the 75 template events.

To reject possible false detections, only events that have been detected independently by at least two stations, and events that have been detected only at CAST but with a minimum correlation coefficient above 0.65, are selected. We also reject families with less than 10 events, as they do not really characterize an active cluster. Finally, we merge families that have common events on different stations. This protocol drastically reduces the total number of detected events to 4909, distributed in 12 different families, all included in the four main clusters A, B, C and D (Table 3 and Figs 4e–f).

This template matching procedure allows us to identify much more events located within the four main clusters (Table 3) than the original and new catalogues. However, most of them cannot be easily located precisely, especially if seen by less than three stations. Therefore, for each family, we estimate a location, by taking the average location of all events included in this family and that have been relocated by double-differences in the new catalogue (Table 3).

Cluster B is divided in two sub-clusters, B1 and B2 (Table 3), as the B families are clearly divided in two groups inside this cluster. Some are activated earlier in October 2020 and are around 5–6 km depth, when others are activated later (since November/December 2020) and are shallower (3–4 km, Figs 4b and e).

The detected events envelopes, recorded on VIEF and RESF for the cluster A and on CAST for the cluster B can be viewed in Fig. 5. The direct observation of signals for the detected events allows a visual check and validation of our template matching procedure. We also observe a relative and progressive variation of the S-P delay, according to the date, for station CAST and for the cluster B (Fig. 5b). This supports the fact that there is a progressive migration inside this cluster B and that the seismicity migrates towards the surface, getting closer to station CAST (Fig. 5b).

This approach using template matching detection therefore allows a better description of the activation time for the different families: for instance, family 10 (B2) is activated in December 2020, although the first event present in our reference catalogue is only on April 2021 (Table 3). It highlights a progressive activation time of the different clusters: cluster A (family 1–3, Table 3, Figs 4 and 6) is first activated in May 2020, then the deeper part of cluster B (B1, Table 3, Figs 4 and 6) in September 2020 at 5.6 km depth, its shallower part (B2, Table 3) in December 2020 at 4.3 km depth, and finally cluster C in December 2020 at around 3 km depth and cluster D in January 2021 at 5 km depth.

Note that for the three families of cluster A, which have been found to be composed of two subclusters from the location procedures (Figs 4c–f), the events are found indifferently in the shallow part (2–3 km) or in the deeper part (5–7 km) of the cluster, which is puzzling. Either the differences in focal depths do not cause a substantial enough change in the waveforms for the events to be classified into distinct families and, therefore, to allow a clear separation between the two subclusters; either the events are in fact all located in a same depth range, and the observed subclustering is an artefact of the location procedure.

7 LOCATION UNCERTAINTIES

Uncertainties and biases in the localization procedure could lead to misinterpret the spatial-temporal changes of the seismicity. At first order, the localization uncertainty can be estimated through the uncertainty provided by NonLinLoc during the localization procedure. For the A cluster, the average depth uncertainty is 2.3 km and the horizontal uncertainty is 1.2 km. For the cluster B, the average depth uncertainty is 1.8 km and the horizontal uncertainty is 1.3 km.

7.1 Location uncertainties from picking uncertainties

We first evaluate the influence of the picking accuracy on the final location, by comparing earthquake locations for the two absolute location methods used (automatic and manual, Figs 2e and f). The epicentral locations are consistent, most of the location differences being within ± 1 km (Figs 2e and f and S1). Most of the events in the cluster B show also depth difference below 1 km. For the cluster A, the depth differences, however, can be quite large (Fig. S1). As already observed, earthquakes are located in two depth ranges for this cluster A: approximately 2–4 km and 5–8 km. These two depth ranges are found from all localization procedures (manual, automatic and automatic-HypoDD), but a given event can be found located in the shallow part from one localization method and in the deeper part from another method (Fig. S1). This is clearly an indication of a lack of robustness of the depth estimation: small picking differences/changes in the localization procedure can lead to two different depth solutions.

7.2 Depth uncertainty for the cluster A

Depth estimation accuracy relies mostly on the distance to the closest stations, the accuracy of picks of *P* and *S* waves on these stations, and on the velocity model accuracy (e.g. Gomberg *et al.* 1990; Bondar *et al.* 2004; Husen & Hardebeck 2010; Bondar & Storchak 2011; Letort 2014). The depth parameter can also have a trade-off with the estimation of the origin time during the localization procedure (e.g. Hussen & Hardebeck 2010; Letort 2014). To evaluate depth estimation for the cluster A, it is therefore interesting to have a closer look at the *P* and *S* arrivals at the closest stations available during the time of the activation of the cluster A, VIEF and RESF.

We remind that most of the events in the cluster A have an exact same S-P delay observed for the two stations (Fig. 5a). We estimate that these delays can vary at most between 1.75 and 1.85 s for RESF and between 2.25 and 2.4 s for VIEF. S-P delays depend on depth, epicentral distance and velocity model. Assuming that the epicentral localizations for the cluster A are well constrained (at 1 km level), and that the velocity model is trustworthy, these S-P delays depend only on depth estimation and can then be used to evaluate which depth range can explain these observed delays. Relying on S-P delays instead of direct *P*- and *S*-wave arrival times allows avoiding issues from possible trades-off between depth and origin time. In Fig. 7(a), we can see that S-P delays varying from 1.75 to 1.85 s on RESF can be compatible with a large depth range according to event distance. For most of the events, at an average distance of 13.5 km, the depths that better explain the S-P delays are varying between 4 and 7 km. For events located only a few hundred metres further from RESF (around 13.8 km), the delays point to depths varying between 0 and 6.5 km. A very small S-P delay variation of less than 0.05 s or an epicentral change of less than 0.5–1 km can therefore lead to different depth solutions. This illustrates that the depth cannot be constrained more precisely. We can only affirm that the events

Table 3. Statistics on the 12 families of events selected after the template matching process (see text). The coordinates refer to the template of each family, and the standard deviations (Std) relate to the differences between events inside a same family.

Cluster	Family No.	Lat (°)	Lon (°)	Depth (km)	Std Lat (km)	Std Lon (km)	Std Depth (km)	No. of ref. events	No. of detec. events	First detec. event in Init. Cat.	First detec. event with Temp. Match.
A	1	42.897	0.234	7.8	0.2	0.5	2.5	14	39	2020-06-03	2020-05-31
A	2	42.900	0.233	3.1	0.1	0.2	1.5	9	35	2020-06-20	2020-06-19
A	3	42.897	0.232	3.6	0.0	0.1	0.1	5	13	2020-07-14	2020-07-14
B1	4	42.922	0.197	5.6	0.2	0.4	1.0	237	2177	2020-09-26	2020-09-22
B1	5	42.923	0.196	5.7	0.2	0.2	0.5	91	334	2020-09-23	2020-09-23
B1	6	42.922	0.195	5.4	0.2	0.2	1.4	85	414	2020-10-14	2020-10-10
B1	7	42.922	0.194	5.2	0.0	0.1	2.1	5	14	2020-10-17	2020-10-17
B1	8	42.919	0.200	6.0	0.1	0.2	0.1	6	29	2020-12-10	2020-12-10
B2	9	42.919	0.193	4.3	0.3	0.3	0.5	84	1377	2020-12-03	2020-12-01
B2	10	42.917	0.195	4.3	0.2	0.4	0.1	14	225	2021-04-22	2020-12-02
C	11	42.888	0.176	3.1	0.2	0.1	1.4	10	231	2020-12-11	2020-12-07
D	12	42.861	0.141	5.2	0.2	0.2	0.5	5	21	2021-01-15	2021-01-19

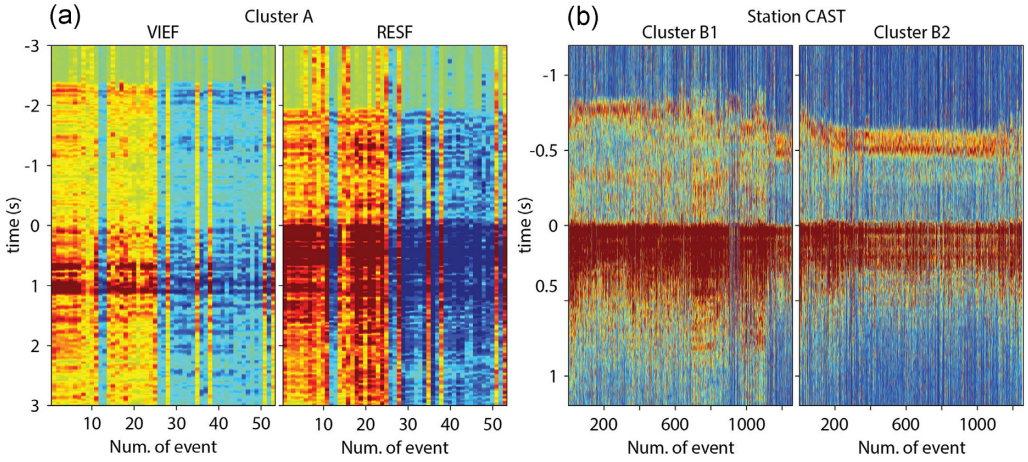

Figure 5. (a) Mean waveform envelopes (normalized by the amplitude of the *P*-arrival) for all the events detected by template matching at cluster A and recorded at VIEF and RESF stations (sum of the three components). Signals are 5–20 Hz bandpass filtered and centred at the *S*-wave arrival time. The red colour scale corresponds to the events of the deeper part of the cluster A (included in the family 1, see Table 3), and the blue colour scale to those of the shallower part (families 2 and 3, Table 3). (b) Envelop of the CAST station signals for both B1 and B2 clusters. Signals are 10–40 Hz filtered, normalized, and sorted by date.

are in the 0–8 km depth range. This observation is consistent with the empirical rule proposed by Gomberg *et al.* (1990): to constrain the depth, we need at least one *S*-wave arrival picked on a station located at an epicentral distance lower than 1.4 time the focal depth. Our closest station RESF is located at 13–14 km to the cluster A. According to Gomberg's rule, it is therefore difficult to constrain the depth for events below 13/1.4 ∼9 km. For VIEF, a large range of depth between 0 and 10 km can then explain a similar S-P delay (Fig. 7b).

7.3 Depth uncertainty for the cluster B

Following the same procedure to evaluate depth estimation for the cluster B, S-P delays observed at station CAST for B1 (0.75–0.95 s) could explain a depth range varying between 4 and 6 km (Fig. 7c). In addition, S-P delays observed at CAST for B2 (0.6–0.7 s) can explain a depth range between 3 and 4 km, which is consistent with that found by the HypoDD procedure, although slightly shallower (Fig. 7d). For this cluster B, variations of S-P delays of 0.1 s and/or epicentral variation of 1 km will yield maximal changes of 1–2 km. Thanks to the location of CAST, just above the cluster B, the depth of this cluster is therefore very well constrained.

7.4 Influence of the velocity model

We also check the robustness of the locations by testing different velocity model. We test homogeneous velocity models, and layered velocity models derived from the Pyrenean model changing only the depth interface of the first and second velocity layer. We show that relatively small changes of the velocity model do not drastically impact the B cluster localizations. Depth and epicentral location are therefore robust for this cluster (Fig. S2). However, when moving the depth of the second layer of the Pyrenean velocity model from 6 to 8 km, most of the earthquakes' depths of the cluster A become deeper and remain localized each time around this varying interface depth (Fig. S2). Once again, this tends to prove that this cluster A depth is not well constrained.

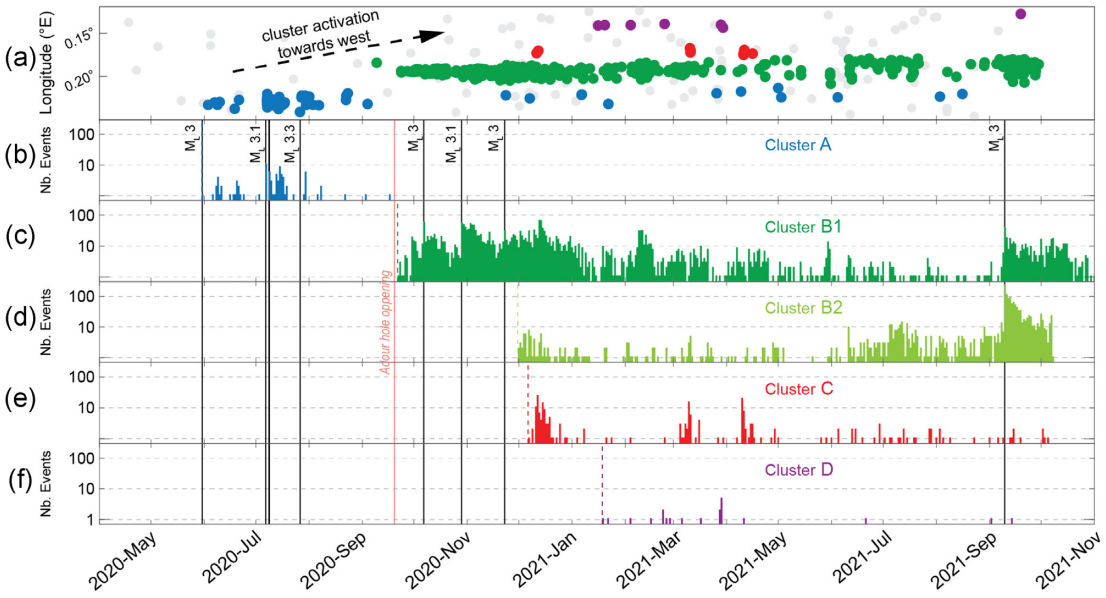

Figure 6. Temporal evolution of the 5 clusters. (a) Longitude of the different events as a function of their date and corresponding cluster labels (PhaseNet reference catalogue). (b–f) Number of events by day for each of the considered clusters A to D using detection by template-matching. The coloured dashed lines indicate the time of the first event for each cluster. Black vertical lines show the date of major events ($M_L \geq 3$). The orange vertical line indicates the date of the appearance of the 'Adour hole'.

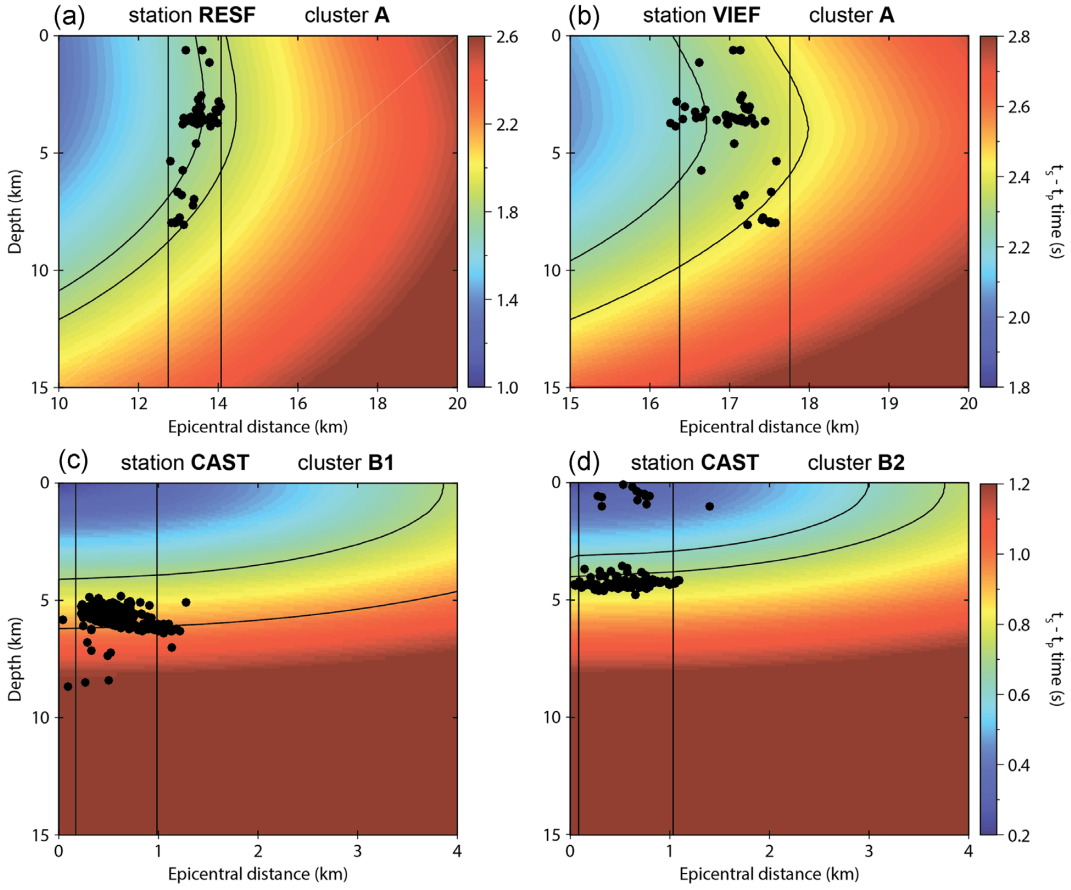

Figure 7. Theoretical time t_S–t_P calculated with our 1-D velocity model as a function of the epicentral distance and the depth, for events of the cluster A (a and b, stations RESF and VIEF, respectively), and for the events of clusters B1 and B2 at station CAST (c and d). Vertical black lines delimit the range of the epicentral distance for the locations estimated with HypoDD. The curvy black lines indicate the range of the differences of t_S–t_P measured on the signals envelops (see Fig. 5).

8 MAIN FEATURES OF THE SEISMIC CRISIS

8.1 Clusters A to D: progressive activation to the west–southwest

A first interesting feature is that the earthquakes appear to migrate west or southwest, with progressive activation of the different clusters (Fig. 6a). Clusters A, B, C and D are located at 0.230°E, 0.195°E, 0.175°E and 0.140°E, respectively (Fig. 4a), and are chronologically activated (dashed lines Figs 6b–f), indicating a clear migration to the west with time. Apart from cluster A, located at 42.900°N, the three other clusters B, C and D also follow a chronological pattern to the south, being located at 42.920°N, 42.890°N and 42.865°N, respectively.

8.2 Cluster B: dipping structure

Focusing on the cluster B, the relative relocations (Fig. 4b) show clearly an extent of the seismicity along a subvertical structure (dip ±75°), with a strike orientation varying between northeast and east–northeast (azimuth 124°). The focal mechanism determined for an event from this cluster B shows a consistent azimuth (326°) and dipping direction (east–northeast, see Section 2, Fig. 2d).

8.3 Cluster B: migration of the seismicity towards surface

Both the relative relocation approach as well as the template matching procedure show that the deeper part of the cluster B is first activated in September 2020 (B1, Figs 4e and 6c), followed by its shallower part, in December 2020 (B2, Figs 4e and 6d). This internal migration pattern can also be observed directly on the event waveforms. In Fig. 5(b) for instance, the average envelopes of the waveforms observed at CAST clearly show that the S-P delay decreases steadily with time. The relative variation of the S-P delay with time is an indication of the migration of the seismicity, which progressively gets closer to the station, and becomes shallower. Interestingly, this direct observation of these S-P delay variations is fully data driven, independent of any bias coming from the localization procedure. It allows noticing a weak but consistent migration pattern towards surface inside the B2-cluster that is not visible from the final catalogue (Fig. 5b).

8.4 Triggering processes

In addition to the observed consistent migration patterns, at least one episode of triggering processes can also be noted. The M_L 3 event of 10 September 2021, which occurred in the shallow part of the cluster B (B2), is followed by an immediate burst of events in both the B2 and B1 clusters (Figs 6c and d). Assuming that the size of the rupture is reasonably lower than 1 km, it seems unlikely that it could have broken the entire area of cluster B over several kilometres. A reactivation of the deeper part of cluster B, dynamically triggered by this major event, seems more likely.

Finally, we can observe bursts of seismic events preceded by a major event in only a few occurrences (M_L 3.1 July 2020, M_L 3 and 3.1 in October 2020 and M_L 3 September 2021, see Figs 6b–d). This lack of main shock-event preceding a burst is one of the prerequisites to define a seismic sequence as a seismic swarm (Horalek *et al.* 2015), and their occurrence are generally attributed to fluid driven processes (e.g. Vidale & Shearer 2006; Chen *et al.* 2012; Gueguen *et al.* 2021), slow-slip processes (e.g. Roland & McGuire 2009) or both of them (e.g. DeBarros *et al.* 2020). In the next section, we investigate the possible role of fluids and triggering processes of these swarms.

9 DISCUSSION—MECHANISMS DRIVING THE SEISMICITY AND STUDY OF THE LINK WITH THE ADOUR HOLE

Considering the initiation of seismicity within the cluster A on May 2020, and the last cluster D, activated in January 2021, the observed migration velocities are of around 1 km per month, that is in the order of few tens of metres per day, which is coherent with fluid driven swarms (Vidale & Shearer 2006; Roland & McGuire 2009; Chen & Shearer 2011; Chen *et al.* 2012; De Barros *et al.* 2020). Despite the lack of geodetic data, which could have allowed us to constrain surface displacements, the aseismic slip is not likely to explain the seismicity around Gripp, as it would have involved migration velocities of two to three orders of magnitude higher (tens of km per day, Lohman & McGuire 2007; DeBarros *et al.* 2020). Following Shapiro *et al.* (2002), we model the geometrical expansion of the swarms as a diffusion process, using a R–T diagram (time t versus absolute distance to the first event r) to estimate the fluid diffusion coefficient D (eq. 1, and Fig. 8).

$$r = \sqrt{4 \prod \mathrm{D}t} \tag{1}$$

From Fig. 8, D ($m^2\ s^{-1}$) can be estimated to be bounded between values of 0.20 and 0.30 $m^2\ s^{-1}$, which is consistent with expected diffusivities estimated by previous studies, ranging from 0.02 to about 10 $m^2\ s^{-1}$ (Shapiro *et al.* 1997, 2002).

This seismic crisis is then probably driven, at first order, by a diffusion of fluids along the identified structures. The progressive activation of the B cluster from its deeper part (B1) towards its shallower part (B2) seems to indicate that fluids are migrating towards the surface. Mechanical triggering processes also seem to be involved, as suggested by the reactivation of the deeper part of the fault (cluster B2) in September 2021 (Figs 6c and d). However, despite the apparent spatial and temporal correlation between the appearance of the cavity along the Adour River and the seismic pattern of the region (see Fig. S3), this process cannot be explained by the diffusion envelope (Fig. 8). We then explore the possible triggering relationship between the seismic activity and the 'Adour hole' by calculating the static Coulomb stress change (ΔCFF). We use the Coulomb3.4 software (Toda *et al.* 2011) with a Young's modulus of 80 GPa, a Poisson's coefficient of 0.25, and a friction coefficient of 0.4 (mean values for calcareous rocks at 5 km depth, Schön 2011). The regional stress field used is that determined for *zone #5* in Rigo *et al.* (2015), that is with strike/plunge of 294/16, 119/73 and 24/1 for σ_1, σ_2 and σ_3, respectively. The considered triggering event is the 31 May 2020, M_L 3, with a focal mechanism corresponding to a NW–SE trending normal fault. Based on the distribution of the east-dipping seismicity, we modelled the NE dipping nodal plane with strike/dip/rake of 326/42/−107, centred at 5 km depth, and with a seismic moment $M_0 = 4.0 \times 10^{13}$ N.m corresponding to a magnitude $M_W = 3.0$. We calculated the ΔCFF at the surface for an optimal normal fault, as we test whether an extensional style of deformation can be triggered at the 'Adour hole' site.

As a result, the ΔCFF at the 'Adour hole' location is very small, of about 20–40 Pa, the order of magnitude of the diurnal atmospheric

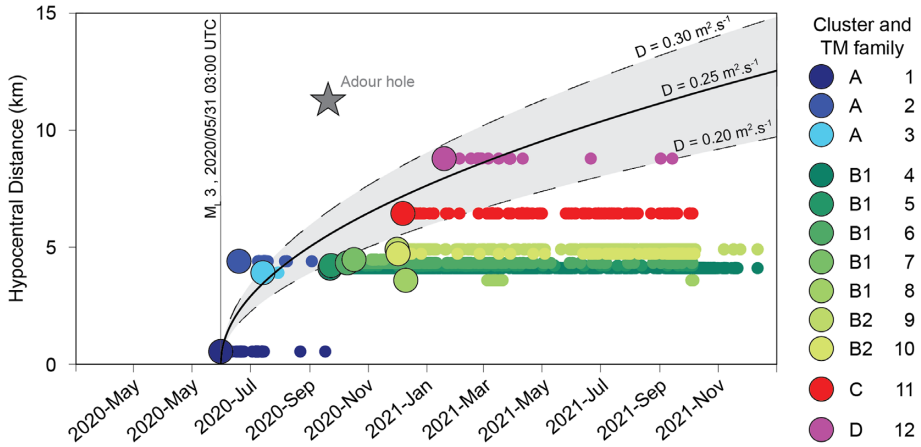

Figure 8. R–T diagram. Hypocentral distance of events to the first cluster according to their origin time for all events detected by template matching. The big circles indicate the first event of each of the 12 families. The diffusivity curves with $D = 0.20$, 0.25 and 0.30 m^2 s^{-1} are plotted in black to highlight the fluid diffusion process occurring.

tide, which is too small to be considered as a valid shallow triggering process. However, the disappearance of the Adour water might be due to a slight and deeply variation of the karst permeability, by changes in fracture's porosity at depth due to small deformations of the karstic volume (e.g. Derode *et al.* 2013; Guglielmi *et al.* 2013). In this case, the calculated dilatation strain of 0.2–0.3 μstr, consistent with the strain values that can trigger karstic phenomena (Toutain & Baubron 1999), can be sufficient to indirectly induce the Adour hole phenomenon.

The appearance of the 'Adour hole' at Sainte-Marie de Campan shows then a spatial and temporal correlation with the recent seismic activity of the Gripp valley, and is furthermore located on a large karst environment, close to the intersection of two tectonic faults (the Adour Fault and the North Pyrenean Fault, Figs 1, 2 and 4). It is unlikely that the Adour hole was triggered by static stress changes due to one of the main earthquakes in the region. However, we could imagine that this superficial hydrological phenomenon triggered itself the seismicity of the cluster B. For instance, the accumulation of superficial water in poro-fractured karsts can change the elastic stress at depth and produce seismicity (e.g. D'Agostino *et al.* 2018). The propagation of the fluid within hydraulically connected fracture system can also change the internal pore pressure and reduce the frictional strength, leading to a fragile rupture along pre-existing faults (e.g. Saar & Manga 2003). In both cases, to be significantly involved in earthquake triggering a few km away, these poroelastic processes generally need to be two or three orders of magnitude higher than that observed in the Adour hole case, where water height of the river before its disappearance was of a few cm, inducing stress modulations of a few tens of Pascals where kPa are involved in other similar cases (Christiansen *et al.* 2007). However, by the play of the pre-existing faults of the karstic region where the Adour hole occurred, the entire zone is probably highly fractured and mechanically damaged, leading to the existence of decametric to kilometric instable heterogeneities hydraulically connected within the surrounding volume (e.g. Derode *et al.* 2013). Furthermore, this zone has already been subjected to the occurrence of other cavities on several occasions. According to Adisson (2008), this same phenomenon has already occurred at least three times in the past, in 1773, 1777 and 1816. In 1777, 10 cavities were opened on about 800 m^2, and a fault of 25 m long and 25 cm wide was even observed. The Adour disappeared completely, only to reappear 6 km downstream, at the level of the locality of Médous. All cavities and the outcropping fracture were quickly filled in to allow the river to return to its normal course. These ancient phenomena and the one observed in 2020 concern the same area, along the Adour de Payolle, one of the two main tributaries that converge to give birth to the Adour. If the cavity opening of 1773 and 1816 are poorly documented, two earthquakes has been felt in 1777 by the local population the day before the disappearance of the Adour (7 December 1777, Adisson 2008). Between 1816 and 2020, no other disappearance of the Adour hole was officially reported, but local rumours speak of a possible disappearance 20 yr ago and/or 50 yr ago. Even if a direct connection between the seismicity of the Gripp valley and the 'Adour hole' is not obvious, these different observations suggest a link between the two phenomena. We could imagine a larger fluid circulation over a wider area and a longer time period, not starting only at the time and location of cluster A, and/or aseismic processes that were not captured by this study.

10 CONCLUSION

This 1.5 yr swarm-distributed seismic sequence highlights a new active zone, previously unseen in seismicity catalogues. The swarm B is close to the PMdBF trace, but if we extend the plane drawn by the swarm towards the surface, we fall a few kilometres SW of the estimated PMdBF trace. It seems therefore unlikely that the cluster B occurs on this known fault. It could be related to the Pierrefitte fault (Fig. 4a), if we assume that this fault extends further to the east than known, but clusters C and D do not seem easily linked to any of these western faults. It seems therefore reasonable to think that new structures/segments are concerned here. According to Lacan & Ortuño (2012), the PMdBF is composed of two segments making up a larger fault, unlike the faults further west, which are all composed of a single segment. This would support the fact that the deformation zone is more complex in this area located at the eastern end of the strong seismicity stripe of the central Pyrenees. It would be consistent with previous observations of a change of direction for the deepening of the seismicity in this area (Rigo *et al.* 2005).

This complex zone could then be strongly fractured, and possibly acts as a mechanical barrier (enhanced by the change in direction), that could explain the presence of three large historical earthquakes (Rigo *et al.* 2005) and thus the possibility of another normal fault structure. Moreover, when analysing our new entire catalogue at larger scale, the new earthquake's locations confirm a deepening of the seismicity along the North Pyrenean Fault, east of the 'Adour hole' (dark red dots Figs 2a and c), in the continuity of the four clusters of the Gripp valley (Fig. 2c). These strong larger-scale lateral variations are also in favour of a fractured and heterogeneous zone.

The origin of the fluids/gas possibly diffused from depth is unknown. However, the Pyrenean Mountains are known for the presence of numerous thermal springs, especially near the North Pyrenean Fault. In particular, the chemistry of the geothermal waters at Bagnères-de-Bigorre shows that hot waters, whose temperature can reach 50 °C, rise from 2 km depth to the surface along pre-existing faults, and actively participate in the dissolution of carbonates, developing the karstic system of the region (Levet *et al.* 2002). The seismicity studied in the Gripp Valley, and the 'Adour Hole' being located a few kilometres upstream of the city of Bagnères-de-Bigorre, we can assume that the geothermal waters present the same patterns and channels within the upper crust with the ascent of deep waters along mechanical weaknesses channels, like faults.

High-resolution 3-D imaging of the whole area, and/or precise location of earthquakes, encompassing a larger region, could perhaps allow a better understanding of this central Pyrenean zone. Precise mapping of this highly fractured area and of its complex faulting system could allow to highlight possible connections between the four clusters and the Adour hole. Additional efforts should therefore be made to better understand the seismic properties of this area, the fault system, the occurrence of these seismic swarms and the associated risk, in a region known for its major historical earthquake of 1660. GNSS stations could be installed to measure with better accuracy possible long-term ground deformations and/or annual ground motions due to karst charge/discharge cycles, to compare with seismicity characteristics. Gas measurements could be also made, as well as seismic and/or magneto-telluric imaging, to identify faults and deep fluids positions.

DATA AND RESOURCES

The seismic catalogue used in this study is available at: https://api.franceseisme.fr/fr/search. Local data used from the temporary instrumentation are available from the authors upon request. The deep-learning algorithm PhaseNet used for the phase picking is provided by Zhu W. at https://github.com/wayneweiqiang/PhaseNet. The relocation of the seismic events were obtained with NonLinLoc software available at https://github.com/alomax/NonLinLoc, and most of the figures were created using MATLAB codes downloadable at https://fr.mathworks.com/products/matlab.html.

SUPPORTING INFORMATION

Supplementary data are available at *GJI* online.

Figure S1. Comparison between the three location methods: the absolute location from the manual pickings, the phasenet-automatic location method and the relative relocation from hypoDD. Panels (a) and (b) for the A-cluster. Panels (c) and (d) for the B-cluster. Red colour corresponds to the 2020 events, and black to the 2021 ones. Triangles correspond to HypoDD relative locations, circles to absolute locations from the manual pickings. The dashed lines represent a location difference of 1 km. Most of the event have a consistent longitude, at less than 1 km (c–d). The depth estimation can however show larger difference, especially in 2020 (red dots) when the temporary network was not fully installed. For the A-cluster, all localization methods find 2 distinct depth ranges: 2–4 km and 6–8 km (a), but an event can be found located in the shallow part from one method and in the deeper one from another method.

Figure S2. West–east cross-section along the B and A clusters, for events located (a) from the Pyrenean velocity model, with the absolute NonLinLoc localization and from the automatic phasenet pickings (see main text), but relying only on the permanent RESIF stations—(b) from an homogeneous velocity model ($V_P = 6.1$ km s^{-1}) and relying on automatic pickings made on all temporary and permanent stations—(c), (d), (e) and (f) from the Pyrenean velocity model, modifying only the depth of the second layer interface (originally at 4 km) respectively at 4, 6, 7 and 8 km and still relying on automatic pickings made on all temporary and permanent stations. The colour (and the size of the dots) scales the NonLinLoc vertical uncertainty, between 1 km (blue) and 3 km (red). The B-cluster is located between approximately 0.18–0.21 in longitude and the A-cluster between 0.21 and 0.24. This figure first illustrates the improvement of the localizations thanks to the use of the temporary network. Without any temporary station, no events are located well than 2 km and the shape of the B-cluster is clearly not well constrained (see a). Relying on all temporary and permanent stations, the B-cluster has always the same eastward deepening, whatever the used velocity model (see c, d, e and f), and with only a systematic 1 km shift towards the surface when using the more different homogeneous velocity model (b). The very shallow cluster above the B-cluster (blue light dots, see c and d) disappears when using the homogeneous velocity model (see b), and is probably a bias coming from the localization procedure, due to the first layer interface at 1 km. The A-cluster is not well constrained, with uncertainties above 2 km, and its average depth vary with the second layer interface depth, from 6 to 8 km (see d, e and f). Here again, we assume that it comes from a bias from the localization procedure, the localizations being found clustered around the depth of the second layer interface.

Figure S3. Seismic density as a function of the date and the hypocentral distance to the Adour hole. The colour scales the seismic density by week at a specific hypocentral distance and date. The light copper colour indicates no seismicity, and black colour to a zone with at least seven earthquakes occurring during the corresponding week.

Please note: Oxford University Press is not responsible for the content or functionality of any supporting materials supplied by the authors. Any queries (other than missing material) should be directed to the corresponding author for the paper.

ACKNOWLEDGMENTS

This work was mainly supported by the CEA-DASE and EPOS-RESIF, a Research Infrastructure (RI) managed by the INSU,CNRS. It is a consortium of 18 French research organisations and institutions, included in the roadmap of the Ministry of Higher Education, Research and Innovation. Résif-Epos RI is also supported by the

Ministry of Ecological Transition. We thank the Editor Margarita Segou and the two anonymous reviewers for their constructive comments and suggestions that strongly improved our paper.

REFERENCES

Adisson, L., 2008. Et l'Adour disparut 177317771816, *Bull. Soc. Ramond*., 195–204.

Ammirati, J.B., Villaseñor, A., Chevrot, S., Easton, G., Lehujeur, M., Ruiz, S. & Flores, M.C., 2022. Automated earthquake detection and local travel time tomography in the SouthCentral Andes (32–35° S): implications for regional tectonics, *J. geophys. Res.,* **127**(4), doi:10.1029/2022JB024097.

Baisch, S., Ceranna, L. & Harjes, H.P., 2008. Earthquake cluster: what can we learn from waveform similarity?, *Bull. seism. Soc. Am.,* **98**(6), 2806–2814.

Barréjot, A., 2020, October 7. *Ce Trou Mystérieux Qui A Englouti L'Adour De Payolle,* LADEPECHE. Retrieved June 6, 2022, from https://www.ladepeche.fr/2020/10/07/cetroumysterieuxquiaengloutiladourdepayolle9122471.php.

Bondár, I., Myers, S.C., Engdahl, E.R. & Bergman, E.A., 2004. Epicentre accuracy based on seismic network criteria, *Geophys. J. Int.,* **156**(3), 483–496.

Bondár, I. & Storchak, D., 2011. Improved location procedures at the International Seismological Centre, *Geophys. J. Int.,* **186**(3), 1220–1244.

Chen, X. & Shearer, P.M., 2011. Comprehensive analysis of earthquake source spectra and swarms in the Salton Trough, California, *J. geophys. Res.,* **116**(B9), doi:10.1029/2011JB008263.

Chen, X., Shearer, P.M. & Abercrombie, R.E., 2012. Spatial migration of earthquakes within seismic clusters in Southern California: evidence for fluid diffusion, *J. geophys. Res.,* **117**(B4), doi:10.1029/2011JB008973.

Christiansen, L., Hurwitz, S. & Ingebritsen, S., 2007. Annual modulation of seismicity along the San Andreas Fault near Parkfield, CA, *Geophys. Res. Lett.,* **34**(4), doi:10.1029/2006GL028634.

D'Agostino, N., Silverii, F., Amoroso, O., Convertito, V., Fiorillo, F., Ventafridda, G. & Zollo, A., 2018. Crustal deformation and seismicity modulated by groundwater recharge of Karst aquifers, *Geophys. Res. Lett.,* **45**(22), 12 253–12 262.

DeBarros, L., Cappa, F., Deschamps, A. & Dublanchet, P., 2020. Imbricatedaseismic slip andfluid diffusion drive aseismic swarm in the Corinth Gulf, *Geophys. Res. Lett.,* **47**(9), doi:10.1029/2020GL087142.

Derode, B., Cappa, F., Guglielmi, Y. & Rutqvist, J., 2013. Coupled seismo-hydromechanical monitoring of inelastic effects on injection-induced fracture permeability, *Int. J. Rock Mech. Min. Sci.,* **61,** 266–274.

Derode, B., Guglielmi, Y., De Barros, L. & Cappa, F., 2015. Seismic responses to fluid pressure perturbations in a slipping fault, *Geophys. Res. Lett.,* **42,** 3197–3203.

Derode, B., Letort, J., Chevrot, S., Lehujeur, M., Sylvander, M., Pauchet, H., Grimaud, F. & Cano, Y., 2021. Apport des réseaux de neurons convolutifs dans la detection et le pointé automatique des phases sismiques regionals pg/Sg dans les Pyrénées, 5Èmes Rencontres Scientifiques et Techniques Résif, Nov 2021, Obernai (67210), France. https://hal.archives-ouvertes.fr/hal03463696.

Gao, D., Kao, H. & Wang, B., 2021. Misconception of waveform similarity in the identification of repeating earthquakes, *Geophys. Res. Lett.,* **48**(13), e2021GL092815, doi:10.1029/2021GL092815.

Gomberg, J.S., Shedlock, K.M. & Roecker, S.W., 1990. The effect of S-wave arrival times on the accuracy of hypocenter estimation. *Bull. seism. Soc. Am.,* **80**(6A), 1605–1628.

Gueguen, P. *et al.*, 2021. Unprecedented seismic swarm in the Maurienne valley (2017–2019) observed by the SISmalp Alpine seismic network: operational monitoring and management, *Collect C. R. Geosci.,* **353**(S1), 517–534.

Guglielmi, Y., Henry, P., Cappa, F. & Derode, B., 2013. Relationships between slow slip, seismicity and fluids leakage during a pressurized fault zone rupture in situ experiment: importance for reservoir/caprock stimulation monitoring and efficiency assessment, in *Proceedings of the 47th U.S. Rock Mechanics/Geomechanics Symposium, ARMA 13-517,* American Rock Mechanics Association, San Francisco, CA.

Hatch, R.L., Abercrombie, R.E., Ruhl, C.J. & Smith, K.D., 2020. Evidence of aseismic and fluid driven processes in a small complex seismic swarm near Virginia City, *Geophys. Res. Lett.,* **47**(4), e2019GL085477, doi:10.1029/2019GL085477.

Horálek, J., Fischer, T., Einarsson, P. & Jakobsdótir, S., 2015. Earthquake swarms, in *Encyclopedia of Earthquake Engineering,* pp. 871–885, eds Beer, M., Kougioumtzoglou, I., Patelli, E. & Au, S-K., Springer.

Husen, S. & Hardebeck, J., 2010. *Earthquake Location Accuracy*. CORSSA.

Lacan, P. & Ortuño Candela, M., 2012. Active tectonics of the Pyrenees: a review, *J. Iberian Geol.,* **38**(1), 9–30.

Letort, J., 2014. Méthodes télésismiques d'estimation de la profondeur des séismes: développements et applications, *Doctoral dissertation*, Grenoble.

Levet, S., Toutain, J.P., Munoz, M., Berger, G., Négrel, P., Jendrzejewski, N., Agrinier, P. & Sortino, F., 2002. Geochemistry of the Bagnères de Bigorre thermal waters from the North-Pyrenean Zone (France). *Geofluids,* **2**(1), 25–40.

Lohman, R.B. & McGuire, J.J., 2007. Earthquake swarms driven by aseismic creep in the Salton Trough, California, *J. geophys. Res.,* **112**(B4), doi:10.1029/2006JB004596.

Lomax, A., Michelini, A. & Curtis, A., 2014. Earthquake location, direct, global-search methods, in *Encyclopedia of Complexity and Systems Science,* ed. Meyers, R., Springer, doi:10.1007/978-3-642-27737-5_150-2.

Lomax, A., Virieux, J., Volant, P. & BergeThierry, C., 2000. Probabilistic earthquake location in 3D and layered models, *Adv. Seismic Event Locat.,* **18,** 101–134.

MartinGrasset, J.J., 1969. *Bref historique Des s Éismes Connus dans Notre Région,* Bulletin de la Société Ramond.

Münchmeyer, J. *et al.*, 2021. Which picker fits my data? A quantitative evaluation of deep learning based seismic pickers, *J. geophys. Res.,* **127,** doi:10.1029/2021JB023499.

Pauchet, H., Rigo, A., Rivera, L. & Souriau, A., 1999. A detailed analysis of the February 1996 aftershock sequence in the eastern Pyrenees, France, *Geophys. J. Int.,* **137**(1), 107–127.

Résif, 1995a. RésifRLBP French Broadband network, Résif RAP strong motion network and other seismic stations in metropolitan France, Résif–Réseau Sismologique et géodésique Français.

Résif, 1995b. RésifRAP French Accelerometric Network, *RESIF – Réseau Sismologique et géodésique Français*.

Retailleau, L. *et al.*, 2022. A wrapper to use a machine-learning-based algorithm for earthquake monitoring, *Bull. seism. Soc. Am.,* **93**(3), 1673–1682.

Rigo, A. *et al.*, 2015. Presentday deformation of the Pyrenees revealed by GPS surveying and earthquake focal mechanisms until 2011, *Geophys. J. Int.,* **201,** 947–964.

Rigo, A., Souriau, A., Dubos, N., Sylvander, M. & Ponsolles, C., 2005. Analysis of the seismicity in the central part of the Pyrenees (France), and tectonic implications, *J. Seismol.,* **9,** 211–222.

Roland, E. & McGuire, J.J., 2009. Earthquake swarms on transform faults, *Geophys. J. Int.,* **178,** 1677–1690.

Saar, M. & Manga, M., 2003. Seismicity induced by seasonal groundwater recharge at Mt. Hood, Oregon, *Earth planet. Sci. Lett.,* **214**(3), 605–618.

Schaff, D.P., *et al.*, 2011. On finding and using repeating seismic events in and near China, *J. geophys. Res.,* **116**(B3), doi:10.1029/2010JB007895.

Schön, J.H., 2011. Elastic properties, in *Physical Properties of Rocks: A Workbook,* Elsevier, pp. 149–243.

Shapiro, S.A., Huenges, E. & Borm, G., 1997. Estimating the crust permeability from fluid injection-induced seismic emission at the KTB site, *Geophys. J. Int.,* **131,** F15–F18.

Shapiro, S.A., Rothert, E., Rath, V. & Rindschwentner, J., 2002. Characterization of fluid transport properties of reservoirs using induced microseismicity, *Geophysics,* **67,** 212–220.

Sylvander, M. *et al.*, 2021. Seismicity patterns in southwestern France, *Compt. Rend. Geosci,* **353,** 79–104.

Toda, S., Stein, R.S., Sevilgen, V. & Lin, J., 2011. Coulomb 3.3 Graphicrich deformation and stress change software for earthquake, tectonic, and volcano research and teaching user guide, U.S. Geological Survey OpenFile Report 2011-1060, Available at: http://pubs.usgs.gov/of/2011/1060/.

Toutain, J.P. & Baubron, J.C., 1999. Gas geochemistry and seismotectonics : a review. *Tectonophysics,* **304,** 1–27.

Toutain, J.P., Munoz, M., Pinault, J.L., Levet, S., Sylvander, M., Rigo, A. & Escalier, J., 2006. Modelling the mixing function to constrain coseismic hydrochemical effects: an example from the French Pyrénées, *Pure appl. Geophys.,* **163,** 723–744.

Vidale, J.E. & Shearer, P.M., 2006. A survey of 71 earthquake bursts across southern California: exploring the role of pore fluid pressure fluctuations and aseismic slip as drivers, *J. geophys. Res.,* **111**(B5), doi:10.1029/2005JB004034.

Wadati, K., 1933. On the travel time of earthquake waves, *Geophys. Mag.,* **10,** 514.

Waldhauser, F., 2001. HypoDD: a computer program to compute double difference earthquake locations, US Geological Survey OpenFile Report 01-113.

Waldhauser, F. & Ellsworth, W.L., 2002. Fault structure and mechanics of the Hayward Fault, California, from double difference earthquake locations, *J. geophys. Res.,* **107**(B3), ESE 3–1-ESE 3-15.

Zhang, M., Ellsworth, W. & Beroza, G., 2019. Rapid earthquake association and location, *Seismol. Res. Lett.,* **90,** 2276–2284.

Zhu, W. & Beroza, G., 2019. PhaseNet: a deep-neural-network-based seismic arrival-time picking method, *Geophys. J. Int.,* **216,** 261–273.